

Femtosecond Infrared Spectroscopy Resolving the Multiplicity of High-Spin Crossover States in Transition Metal Iron Complexes

Clark Zahn,* Mariachiara Pastore, J. Luis Perez Lustres, Philippe C. Gros, Stefan Haacke, and Karsten Heyne*



Cite This: *J. Am. Chem. Soc.* 2024, 146, 9347–9355



Read Online

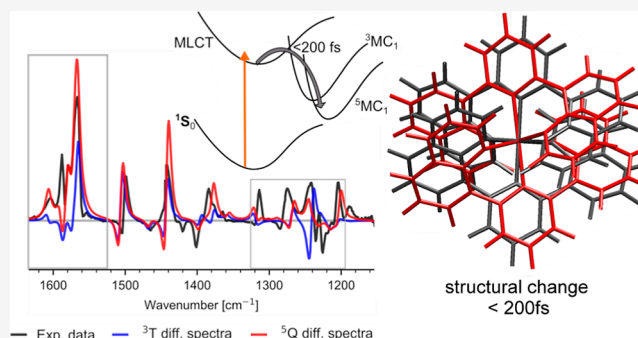
ACCESS |

Metrics & More

Article Recommendations

Supporting Information

ABSTRACT: Tuning the photophysical properties of iron-based transition-metal complexes is crucial for their employment as photosensitizers in solar energy conversion. For the optimization of these new complexes, a detailed understanding of the excited-state deactivation paths is necessary. Here, we report femtosecond transient mid-IR spectroscopy data on a recently developed octahedral ligand-field enhancing $[\text{Fe}(\text{dqp})_2]^{2+}$ (C1) complex with dqp = 2,6-diquinolylpyridine and prototypical $[\text{Fe}(\text{bpy})_3]^{2+}$ (C0). By combining mid-IR spectroscopy with quantum chemical DFT calculations, we propose a method for disentangling the $^5\text{Q}_1$ and $^3\text{T}_1$ multiplicities of the long-lived metal-centered (MC) states, applicable to a variety of metal–organic iron complexes. Our results for C0 align well with the established assignment toward the $^5\text{Q}_1$, validating our approach. For C1, we find that deactivation of the initially excited metal-to-ligand charge-transfer state leads to a population of a long-lived MC $^5\text{Q}_1$ state. Analysis of transient changes in the mid-IR shows an ultrafast sub 200 fs rearrangement of ligand geometry for both complexes, accompanying the MLCT \rightarrow MC deactivation. This confirms that the flexibility in the ligand sphere supports the stabilization of high spin states and plays a crucial role in the MLCT lifetime of metal–organic iron complexes.



INTRODUCTION

Transition-metal complexes are a class of photosensitizers with versatile applications in many fields including solar energy conversion.^{1–4} However, many promising complexes rely on scarce, expensive, and toxic central metals, such as ruthenium or iridium.^{5,6} Thus, recent advancements brought forth new iron-based transition-metal complexes.^{7–23} However, for many newly synthesized iron compounds, including different Fe(II) polypyridyl complexes, the initial excited metal-to-ligand charge-transfer (MLCT) state is deactivated into a high spin metal-centered (MC) state on a subpicosecond timescale.^{19,24–26} Yet, a long MLCT lifetime is mandatory for employing iron transition metal complexes as efficient photosensitizers. An important parameter for tuning the MLCT lifetime is the ligand-field splitting.^{19,27,28} Indeed, enhancement of the ligand-field splitting can lead to destabilization of the high-spin MC state, thus prolonging the MLCT lifetime. One way to achieve this is by promoting an octahedral coordination of the central metal, which reduces the angular strain on the metal center. We recently tried to achieve this with a $[\text{Fe}(\text{dqp})_2]^{2+}$ (C1) complex with dqp = 2,6-diquinolylpyridine (see Figure 1 upper panel), accomplishing an almost ideal octahedral ligand-field enhancing geometry.¹⁹ However, upon excitation of C1, the MLCT state was found to relax on a sub-picosecond timescale into a low-energy MC

state, which we tentatively assigned to the quintet MC state ($^5\text{Q}_1$). Unfortunately, the UV/VIS data did not allow for a clear differentiation between $^5\text{Q}_1$ and $^3\text{T}_1$. In previous work on different Fe(II) polypyridyl complexes, the assignment of the long-lived MC state and possible intermediates proved to be challenging, requiring extensive research and expensive methods.²⁹ In this regard, proto-typical $[\text{Fe}(\text{bpy})_3]^{2+}$ (C0) (see Figure 1 upper panel) was established as a well-investigated benchmark system^{25,26,30–38} for Fe(II) transition-metal complexes.

Here, we report on the femtosecond transient mid-IR spectroscopy study of both C0 and C1, covering the ligand fingerprint region in the spectral range from 1620 to 1180 cm^{-1} . Even though it suffers from a lower time resolution compared to that of the spectroscopy study in the visible or UV range, infrared spectroscopy is particularly sensitive to structural changes, making it well suited for the investigation of MLCT and MC states and potentially distinguish between

Received: February 1, 2024

Revised: March 9, 2024

Accepted: March 11, 2024

Published: March 23, 2024



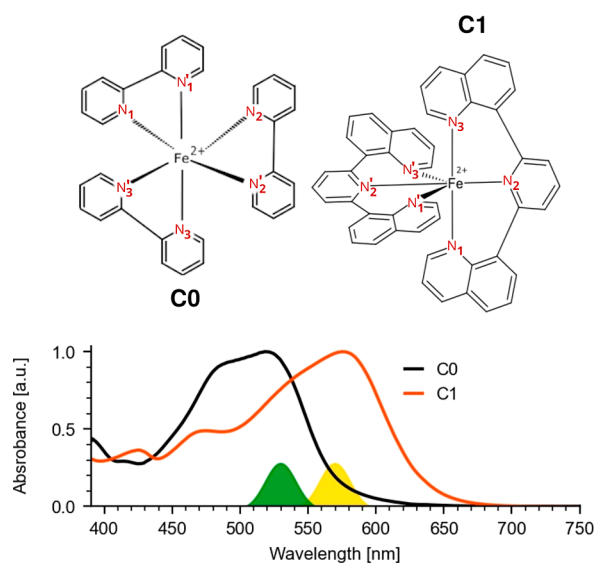


Figure 1. Chemical structure of C0 and C1 (upper panel). Labeling of the coordinating nitrogen atoms highlighted in red color (the counteranion was PF_6^- in both cases). Normalized visible absorption spectrum of the two complexes C0 and C1 (lower panel). Spectral positions of the visible excitation pulses at wavelengths 530 nm (C0, green-filled curve) and 570 nm (C1, yellow-filled curve) are indicated.

various spin multiplicities. However, few reports of femto-second infrared spectroscopy on transition-metal complexes are available.^{30,39–41} Particularly, for the ligand fingerprint region, no in-depth investigation of the long-lived MC states has been reported. We excited the sample to an MLCT state, and within our time resolution, we traced relaxation dynamics in the MC state. We show for the first time that the combination of experimental results and DFT IR spectra calculations allows for a direct assignment of the multiplicity of the observed long-lived MC states.

MATERIALS AND METHODS

Sample Preparation. $[\text{Fe}(\text{bpy})_3]^{2+}$ (C0) and $[\text{Fe}(\text{dqp})_2]^{2+}$ (C1) with dqp = 2,6-diquinolylypyridine were prepared according to refs 19 and 42, respectively; the counteranion was PF_6^- in both cases. Both samples were dissolved in deuterated acetonitrile and prepared in sample cells with a thickness of 100 μm with an absorption of 0.7–0.9 OD at 530 and 570 nm, respectively.

Transient Absorption. Femtosecond laser pulses were generated starting from pulses delivered by a commercially available 1.088 kHz Ti/Sa laser system (Coherent Legend USP, 80 fs pulses at 808 nm). Spectrally tunable visible pump pulses were generated by a home-built two-stage NOPA generating output pulses of $\sim 15 \mu\text{J}$. An AOPDF pulse shaper (Fastlite, Dazzler) compresses the output pulses to (60 ± 20) fs. A $\lambda/2$ -plate was used to set the polarization of the pump-beam, alternating between perpendicular and parallel pump–probe configuration. The isotropic signal was obtained from parallel and perpendicular signals, as follows: $A_{\text{iso}} = (A_{\parallel} + 2A_{\perp})/3$. Here, we show isotropic signals. Before exciting the sample, the pump-pulses were attenuated to 0.2–0.5 μJ . The diameter of the pump beam on the sample was $(180 \pm 40) \mu\text{m}$ (fwhm). IR probe beams with an energy of 50 nJ were generated, as reported elsewhere.⁴³ The generated IR beam was split into two reflections, one acting as the probe beam and the other as a reference. Both beams passed through the same sample volume, with the reference pulse arriving 1.5 ns before the probe, reducing the shot-to-shot signal-to-noise ratio.⁴⁴ Both IR pulses are detected by dispersing the beams with an imaging spectrograph and recording both beams simultaneously with a 128 \times 128 element MCT-array (2DMCT from PhaseTech). The spectral

resolution was better than 3 cm^{-1} . The system response duration and time-zero position were determined using a germanium wafer, yielding $\Delta t = (170 \pm 50)$ fs. The sample was moved with a Lissajous scanner to ensure a fresh sample volume between consecutive pump pulses. The probe pulses were delayed by using a mechanical translation stage.

Data Analysis. The data analysis was performed in Python using the skultrafast^{44,45} package.

Computational Methods. For the quantum mechanical calculations, we used the level of theory validated in a previous work reported by some of us¹⁹ and summarized in the following. Geometry optimization without any symmetry constraint and frequency calculations for the singlet ground state ($^1\text{S}_0$) and the triplet ($^3\text{T}_1$) and quintet ($^5\text{Q}_1$) excited states were carried out by DFT calculations employing the B3LYP exchange and correlation functional and a 6-31+G(d,p) basis set; empirical Grimme's D3 corrections were also applied.⁴⁶ The unrestricted Kohn–Sham formalism was adopted for the open-shell electronic solutions. Solvent effects (acetonitrile) were modeled by using the polarizable continuum model, as implemented in the Gaussian 16 suite of programs.⁴⁷

RESULTS AND DISCUSSION

Normalized steady-state visible absorption spectra of C0 and C1 are shown in Figure 1, lower panel. Both complexes display dominant broad visible absorption bands ranging from 430 to 570 nm (C0, black line) and 440 to 650 nm (C1, orange line).

Transient mid-IR absorption data of the two complexes C0 and C1 are shown in Figure 2a,b, respectively. Positive

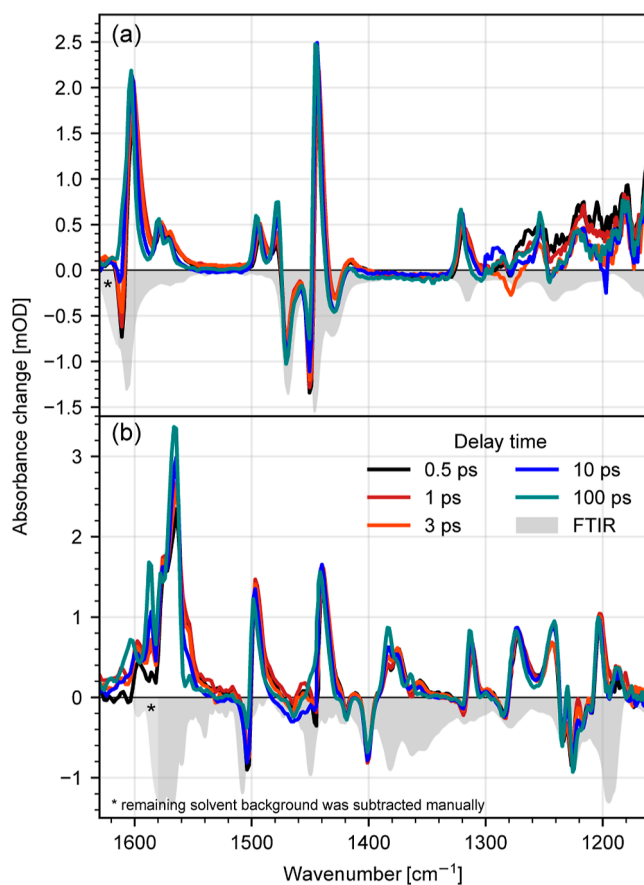


Figure 2. Transient visible pump–mid-IR probe spectra of the complexes C0 (a) and C1 (b) for selected delay times. The ground-state absorption spectrum is indicated by the inverted and scaled FTIR spectra (light gray) for both complexes. The color code for selected delay times is identical for C0 (a) and C1 (b).

contributions are associated with excited-state absorption (ESA), while negative signal shows bleaching of the respective ground-state vibration. The complexes were excited around their visible absorption maxima at 530 nm (C0) and 570 nm (C1), as indicated in Figure 1. Upon excitation, both complexes show strong spectral changes in the fingerprint region from 1150 to 1630 cm^{-1} , attributed to structural reorganization of the ligands. Bands in the range from 1600 to 1400 cm^{-1} are associated with different combinations of $\nu(\text{CN})$ and $\nu(\text{CC})$ stretching modes, while the lower energetic region down to 1150 cm^{-1} shows changes in the ring deformation and C–H bending modes.

Analysis of the polarization-resolved signal shows no significant anisotropy for both C0 and C1 after the system response in the MC state (see Supporting Information Figure S1). This is most likely attributed to a loss of the initial photoselection due to the high symmetry of the ligands or delocalization of the MLCT state. This is in line with previous work on $[\text{Ru}(\text{bpy})_3]^{2+}$, reporting a loss of anisotropy on a timescale of a few hundred femtoseconds.⁴⁸

Vibrational Dynamics. The MLCT to MC transition is reported to happen on a timescale of sub-50 fs²⁶ and ~ 450 fs (upon excitation at 400 nm)¹⁹ for C0 and C1, respectively. For C0, this is out of the range of our system response of (170 ± 50) fs. For C1, we find no ultrafast dynamics on a 0.4–1 ps timescale, suggesting that excitation at 570 nm leads to faster MLCT \rightarrow MC deactivation. Inspection of the early sub-300 fs dynamics at around 1430 cm^{-1} indicates an early evolution of the signal on a timescale of 200–250 fs (see Supporting Information Figure S3), suggesting MLCT \rightarrow MC deactivation on that timescale. Unfortunately, this is not resolvable with our time resolution. Supplementary vis-pump–vis-probe measurements reveal a MLCT \rightarrow MC deactivation with (110 ± 10) fs excited at 550 nm (see Supporting Information Figure S4). Thus, we conclude that the earliest spectra resolved in the mid-IR experiment reported here already correspond to the MC manifold.

Following the MLCT \rightarrow MC transition, both complexes C0 and C1 show significantly stronger ESA signals compared to bleaching signals. This demonstrates an increase of oscillator strength for the vibrational modes in the excited states compared with that in the ground state. This is rather unusual since molecules such as corroles⁴⁹ or chlorophyll a⁵⁰ exhibit similar vibrational signal strengths in the electronic excited state compared to its ground state. Compared to these photoactive systems, the binding forces between iron and ligands in C0 and C1 are rather weak, so that the higher flexibility of the complexes enables an ultrafast rearrangement of ligand geometry, changing bond distances, angles, and dipole moments. Thus, we assign the observed increase of oscillator strength in the electronic excited state to a structural rearrangement of the ligands in combination with a dipole moment change due to partial charge redistribution. These changes occur faster than our time resolution of (170 ± 50) fs, showing that the structural rearrangements happen on a sub-200 fs timescale, in the MLCT state or concomitant with the MLCT \rightarrow MC conversion.

Transient changes on the picosecond timescale for selected wavenumbers are shown in Figure 3a,b. After 30 ps, no relevant changes in the excited state are observed in the investigated time window ranging up to 150 ps. For both complexes, we observe a 2-fold evolution of the signal, with a short time constant of a few picoseconds and a second slower

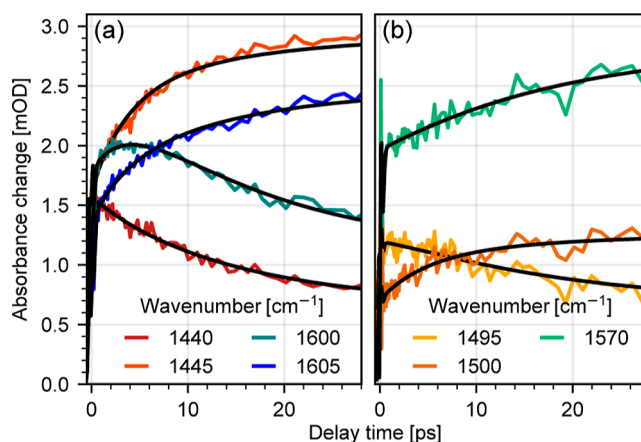


Figure 3. Transient traces for C0 (a) and C1 (b) at selected spectral positions. Black lines show modeling of the data, obtained from global fitting with two exponential decay functions and a constant term.

component with 10–20 ps (see selected transients, Figure 3). Thus, we modeled the spectral dynamics with global analysis using a model of two exponential decay functions $A_{\tau_1, \tau_2}(\nu) \cdot \exp\left(-\frac{t}{\tau_{1,2}}\right)$ and a constant $c(\nu)$. In the case of C0, this yields values of $\tau_1 = (4 \pm 1)$ ps and $\tau_2 = (14 \pm 1)$ ps. Corresponding decay associated spectra (DAS) showing the amplitudes $A_{\tau_1, \tau_2}(\nu)$ are displayed in Figure 4a. Inspection of

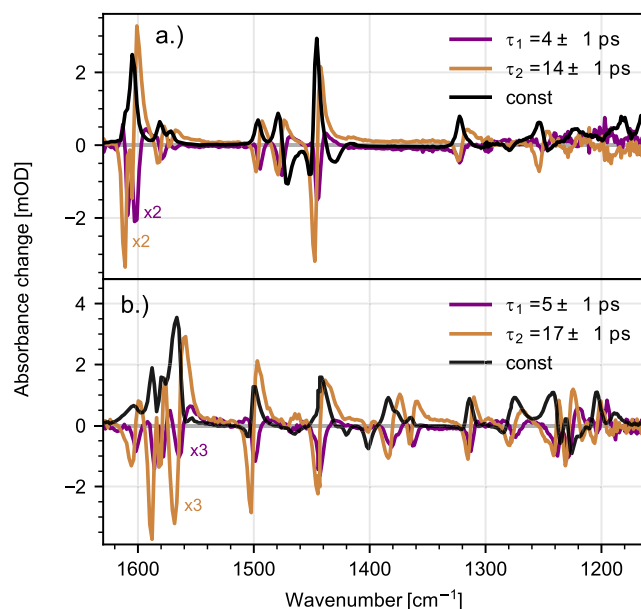


Figure 4. Mid-IR DAS of C0 (a) and C1 (b) obtained from global fitting with two exponential decays. DAS for both C0 and C1 (purple and orange lines) are attributed to fast intramolecular energy redistribution and vibrational cooling. For better visibility, DAS of C0 and C1 are multiplied by a factor of 2 and 3, respectively.

the DAS values for τ_1 and τ_2 exhibits a series of positive and negative peaks. This pattern of positive and negative peaks reflects a blue shift and narrowing of the peaks, well visible in the decrease of signal at 1440 and 1600 cm^{-1} and associated increase of signal at 1445 and 1605 cm^{-1} (see Figure 3a).

These spectral features are typical for intramolecular redistribution of excess energy and energy relaxation associated

with dissipating the energy to low-frequency modes.⁵¹ Thus, we assign both the short time constant of $\tau_1 = (4 \pm 1)$ ps and the second time constant of $\tau_2 = (14 \pm 1)$ ps to dissipation of excess energy to low-frequency modes and subsequent cooling of the low-frequency modes in the MC state.

Comparing our results to previous studies, the fast decay time of (4 ± 1) ps agrees well with the observed time constant of 3.4 ps by Auböck and Chergui,²⁶ while other studies using femtosecond X-ray absorption near edge structure (XANES) and ultrafast electron diffraction (UED) observe faster time constants of (1.1 ± 0.2) ps (XANES),³³ 1.6 ps (XANES),³⁴ and (2.4 ± 0.4) ps (UED).³⁷ For the slower component of $\tau_2 = (14 \pm 1)$ ps, the observed dynamics are not within the measured delay times of both XANES studies^{33,34} and are not detected in the UED study.³⁷ On the other hand, prior work of Smeigh et al.³⁰ using femtosecond-stimulated Raman scattering reveals a slow component of (10 ± 3) ps but missing a fast component. Another study using femtosecond transient absorption by Miller and McCusker³⁶ reports that vibrational cooling is observed with ~ 5 –10 ps. However, these small discrepancies in the obtained time constants are not very surprising. Global analysis using a simple exponential model is generally not sufficient to model complex cooling dynamics.^{52,53} Particularly, cooling-induced blue shifts and narrowing of bands are not well modeled.⁵³ Therefore, we performed a lifetime density analysis (LTDA),^{44,45} fitting a series of i fixed exponentials $A_i(\nu) \cdot \exp\left(-\frac{t}{\tau_i}\right)$ to the data set. Corresponding lifetime density maps (LTDMs) for C0 and C1 applying LTDA with a set of 50 logarithmically distributed time points τ_i are shown in Figure 5a,b, respectively.

Negative and positive amplitudes, $A_i(\nu)$, are displayed in orange and purple, respectively. Sum of all contributions for the whole spectral range is displayed in the left panel of the figure. Inspection of the LTDM reveals the complex nature of the underlying processes. In line with the DAS, adjacent diagonal positive and negative contributions reflect a blue shift and narrowing of the bands. On the other hand, LTDA reveals the nonexponential behavior of the vibrational relaxation dynamics, well visible in the smeared out contributions ranging between 10 and 20 ps, as depicted left in the panel of Figure 5a.

After energy redistribution and vibrational relaxation, the complex is in the thermally equilibrated MC state. The associated spectrum is represented by the constant contribution of the DAS (black line in Figure 4a).

For C1, global analysis yields time constants of $\tau_1 = (5 \pm 1)$ ps and $\tau_2 = (17 \pm 1)$ ps. Associated DAS are depicted in Figure 4b, while the results of LTDA and associated LTDM are presented in Figure 5b. The results reveal very similar vibrational relaxation dynamics for C1 as for C0. In short, after initial population of the MLCT state, ultrafast ISC leads to deactivation of the MLCT and population of the MC state accompanied by structural rearrangement. This is the first state resolved in the IR transient absorption data. Afterwards, redistribution of excess energy to low-frequency modes leads to shifting and narrowing of the positive signals, well visible in the decrease of signal at 1495 cm^{-1} and increase of signal at 1500 cm^{-1} (Figure 3b). LTDA highlights the nonexponential behavior of the vibrational relaxation dynamics, revealing vibrational relaxation dynamics occurring between 10 and 20 ps. The remaining signal is attributed to the thermally

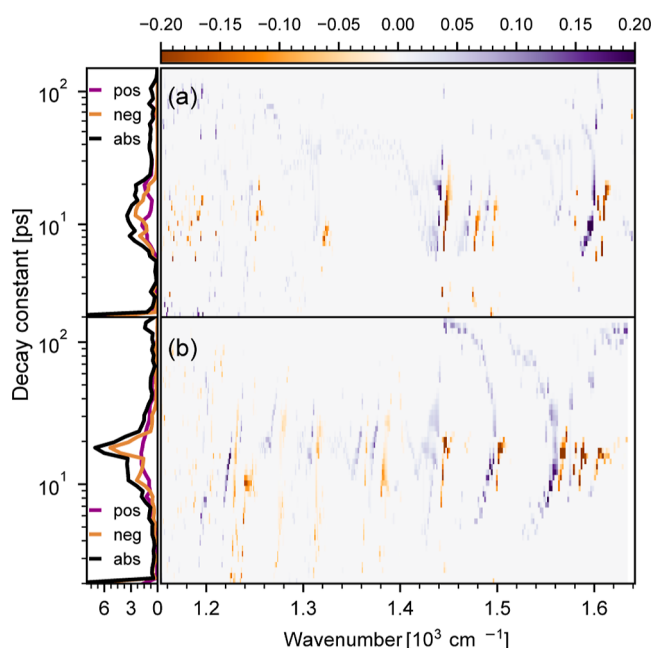


Figure 5. LTDMs of C0 (a) and C1 (b). LTDA was performed with a set of 50 logarithmically distributed time points τ_i . On a timescale of 10–20 ps, both complexes exhibit pairs of negative and slightly blue-shifted positive contributions; with increasing decay times, the pairs shift to higher frequencies indicating red shift and cooling of vibrations; positive decaying signals show a stronger distribution of decay times due to narrowing of the vibrational bands. These dynamics are attributed to energy redistribution and vibrational relaxation.

equilibrated MC state, represented by the constant DAS of C1 (see the black line in Figure 4b).

Coherent Oscillations. Closer inspection of the transient mid-IR absorption of the $\nu(\text{CN})$ and $\nu(\text{CC})$ stretching bands at 1570 – 1610 cm^{-1} of C0 reveals coherent oscillations. Transient traces of selected wavenumbers are depicted in Figure 6a. In order to characterize the coherent motion, we modeled the data using an exponentially decaying cosine function convoluted with a Gaussian function representing the instrument response function. This yields frequencies of 73 – 121 cm^{-1} and 61 – 105 cm^{-1} , with damping times of (300 ± 100) fs and (200 ± 100) fs, at 1589 and 1593 cm^{-1} , respectively. We assign the coherent oscillation to the formation of a vibrational wave packet in the $^5\text{Q}_1$ state, changing the Fe–N coordination. Our results agree well with previous work of Auböck and Chergui²⁶ (Vis TA), Lemke et al.³⁴ (XANES), and Zang et al.⁵⁴ (femtosecond X-ray fluorescence spectroscopy), all three studies showing clear coherent oscillations attributed to the breathing modes of the Fe–N coordination sphere.

For C1, inspection of the transient mid-IR absorption at around 1430 – 1440 cm^{-1} shows small coherent oscillation close to our S/N level and experimental time resolution. However, Fourier analysis of the residuals indicates an oscillating feature with a frequency of 150 – 200 cm^{-1} (see Figure 6b). This matches well with the low-frequency modes modeled by our quantum chemical calculations, at 145 , 197 , 199 , and 202 cm^{-1} . Atomic displacements of the low-frequency modes are shown in Supporting Information Figures S7 and S8. All four modes are associated with vibrations in the Fe–N coordination sphere, similar to that of C0. The Fourier analysis

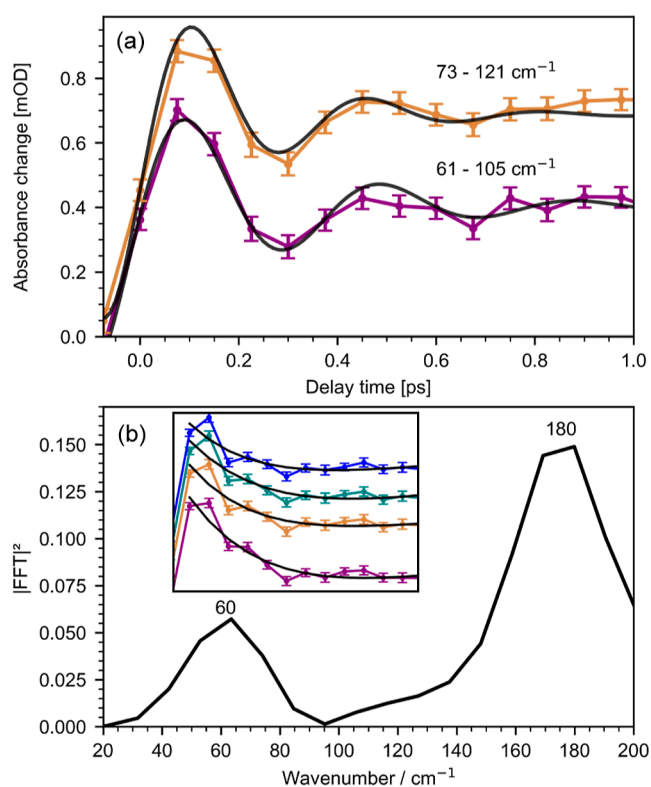


Figure 6. (a) Transient traces of C0 revealing coherent oscillations with frequencies of 73–121 cm^{-1} (at 1593 cm^{-1} , orange line) and 61–105 cm^{-1} (at 1589 cm^{-1} , purple line). Damping is modeled with (300 ± 100) fs (at 1589 cm^{-1}) and (200 ± 100) fs (at 1593 cm^{-1}). (b) Fourier analysis of the residuals after fitting a biexponential decay to selected transients at 1430–1436 cm^{-1} of C1 (inset). Fourier analysis reveals dominant oscillating features at 150–200 cm^{-1} and small contributions at 40–80 cm^{-1} .

also shows contributions at 40–80 cm^{-1} , in line with the results reported by Darari et al.,¹⁹ showing a clear coherent oscillation with 53–65 cm^{-1} . Here, our quantum chemical calculations give three possible associated low-frequency modes at 66, 70, and 82 cm^{-1} . All of these modes show clear ligand deformation, affecting the Fe–N coordination sphere.

Multiplicity of the MC State. In order to determine the multiplicity of the long-lived MC state in C0 and C1 and to distinguish between the $^3\text{T}_1$ and $^5\text{Q}_1$ states, we performed quantum chemical calculations. From the calculations, we obtain the respective $^1\text{S}_0$, $^3\text{T}_1$, and $^5\text{Q}_1$ state infrared spectra and compare the theoretical results to the experimental data. For a detailed analysis of the individual spectra, see the Supporting Information (Figure S6 and Tables S1 and S2). Geometry-optimized structures for the ground-state $^1\text{S}_0$ (green), $^3\text{T}_1$ state (blue), and $^5\text{Q}_1$ state (red) for both complexes C0 and C1 are presented in Figure 7a,b insets, respectively.

Optimized structures for C0 show that both the $^3\text{T}_1$ and $^5\text{Q}_1$ states exhibit different geometries with longer Fe–N distances compared to the $^1\text{S}_0$ state (see Table 1). This is expected as these are antibonding states. On the other hand, the two high spin states $^3\text{T}_1$ and $^5\text{Q}_1$ have a very similar geometries with only subtle differences. Thus, the two high spin states cannot be easily distinguished, as shown in Figure 7a.

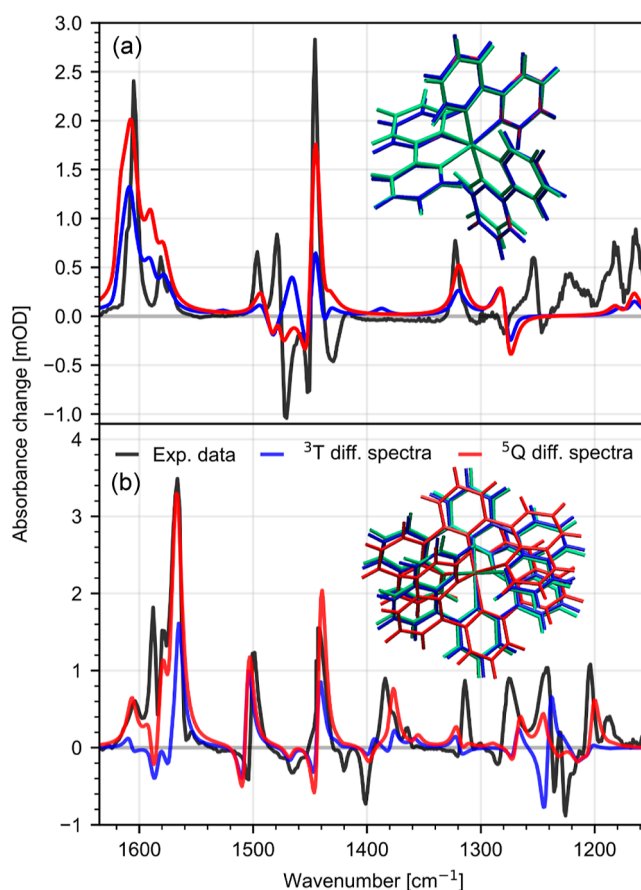


Figure 7. Experimental difference spectra (black) of the thermally equilibrated MC state of C0 (a) and C1 (b). Theoretical spectra are obtained using a Lorentzian convolution with a width of 5 cm^{-1} and a vibrational frequency scaling factor of 0.98, matching the experimental and theoretical spectra. Theoretical difference spectra are calculated for the triplet MC $^3\text{T}_1$ ($^3\text{T}_1 - ^1\text{S}_0$) (blue) and quintet MC $^5\text{Q}_1$ ($^5\text{Q}_1 - ^1\text{S}_0$) (red). Inset: stick representation of the geometry-optimized structures of C0 and C1 for the ground-state $^1\text{S}_0$ (green), $^3\text{T}_1$ state (blue), and $^5\text{Q}_1$ state (red). C0 shows very little structural difference between $^3\text{T}_1$ and $^5\text{Q}_1$ configurations.

Table 1. Fe–N Distances (in Å) from Geometry-Optimized Structures of the $^1\text{S}_0$, $^3\text{T}_1$, and $^5\text{Q}_1$ States^a

Fe–N	$^1\text{S}_0$	$^3\text{T}_1$	$^5\text{Q}_1$
C0			
Fe–N1	2.000	2.170	2.198
Fe–N2	2.000	2.148	2.163
Fe–N3	2.000	1.985	2.178
Fe–N1'	2.000	1.993	2.168
Fe–N2'	2.000	2.300	2.190
Fe–N3'	2.000	2.085	2.173
C1			
Fe–N1	2.024	2.160	2.191
Fe–N2	2.000	1.980	2.160
Fe–N3	2.025	2.161	2.198
Fe–N1'	2.025	2.160	2.191
Fe–N2'	2.000	1.980	2.160
Fe–N3'	2.025	2.161	2.198

^aThe atom labeling is reported in Figure 1.

For C1, all three states have clearly different geometries. These changes in the ligand orientation directly impact the

coordination spheres surrounding the central iron atom, affecting the Fe–N distance. Changes in the Fe–N distance for both complexes **C0** and **C1** are presented in Table 1. These structural differences, particularly the lengthening of the iron–ligand bond, lead to a change in the force constants, particularly for the N–C stretching vibrations. These changes in force constants have a direct impact on the normal modes of the complexes. We performed normal-mode analysis and determined the associated infrared spectra for the respective geometry. In order to compare the theoretical results with the experimental data, we calculated the theoretical difference spectra of 3T_1 (${}^3T_1 - {}^1S_0$) and 5Q_1 (${}^5Q_1 - {}^1S_0$), as shown in Figure 7. Experimental MC difference spectra of the thermally equilibrated MC state are shown in black. By comparing the calculated difference spectra of **C0** for multiplicities 3T_1 (blue line) and 5Q_1 (red line), we observe clear differences at around 1450 cm^{-1} as well as minor differences at around 1600 cm^{-1} . Comparison with the experimental data (black line) shows that the experimental spectrum agrees better with the 5Q_1 difference spectrum than with the 3T_1 difference spectrum. This is best visible in the region between 1440 and 1520 cm^{-1} . Further, at 1480 cm^{-1} , the experimental data show a clear negative bleaching signal, matching the negative signal of the 5Q_1 difference spectrum. In contrast, the difference spectrum associated with 3T_1 shows a positive contribution. In general, for the spectral region between 1440 and 1520 cm^{-1} , we find that even though the individual band intensities are different, the 5Q_1 difference spectrum matches the experimental data noticeably better than the 3T_1 difference spectrum.

In the case of **C1** (Figure 7b), comparison of the calculated difference spectra of 3T_1 (blue line) and 5Q_1 (red line) reveal clear differences at around 1600 cm^{-1} and between 1200 and 1300 cm^{-1} , indicating spin-sensitive marker bands at 1570 – 1620 cm^{-1} and 1200 cm^{-1} . Particularly, the modes at around 1600 cm^{-1} , associated with C–N stretching vibrations, are expected to be very sensitive to the difference in geometry between 3T_1 and 5Q_1 . Considering the experimental data, we find that the 5Q_1 difference spectrum agrees much better with the experimental MC spectrum than the 3T_1 difference spectrum. For example, the positive signal at 1570 – 1620 cm^{-1} is well represented in the 5Q_1 difference spectrum, while it is absent in the 3T_1 difference spectrum. Likewise, the two positive peaks at 1240 and 1280 cm^{-1} agree well with the 5Q_1 difference spectrum, whereas the 3T_1 difference spectrum shows an opposite negative signal at 1240 cm^{-1} . This allowed us to assign the long-lived component of **C1** to the 5Q_1 state.

However, for **C0**, the picture is not as clear since the striking differences are limited to a small spectral region, as discussed above. Thus, in addition to the inspection of individual bands, we determined the overlap between the experimental and the calculated spectra in order to quantify the agreement. For this, we multiplied the experimental signal A_{exp} with the signal of the respective calculated difference spectra A_{theo} for both spin states 3T_1 and 5Q_1 and averaged it over the whole spectral region. This yields an overlap factor f

$$f = \sum_{\nu} \frac{A_{\text{exp}}(\nu) \cdot A_{\text{theo}}(\nu)}{N_{\nu}} \quad (1)$$

where N_{ν} is the number of data points. The larger the value of f , the better the agreement. The calculated overlap factors for both complexes are **C0**: (3T_1 :0.041)/(5Q_1 :0.088) and **C1**: (3T_1 :0.036)/(5Q_1 :0.157). The results show that for **C0**, the

overlap of 5Q_1 with the experimental data is twice that of 3T_1 , and for **C1**, the overlap of the 5Q_1 is even four times the overlap factor of 3T_1 . With this, we assign the long-lived component of **C0** to the 5Q_1 state. This is consistent with the established assignment.^{25,30,32,34} For **C1**, the clearly better overlap of experimental and calculated spectra corroborates our initial assignment toward the 5Q_1 state.

Electron Densities of 3T_1 and 5Q_1 . The MC character of the 3T_1 and 5Q_1 states becomes apparent in the changes in the electron density for the ${}^1S_0 \rightarrow {}^3T_1$ and ${}^1S_0 \rightarrow {}^5Q_1$ transition obtained from B3LYP electronic structure calculations, as depicted in Figure 8. Dark gray color is associated with charge

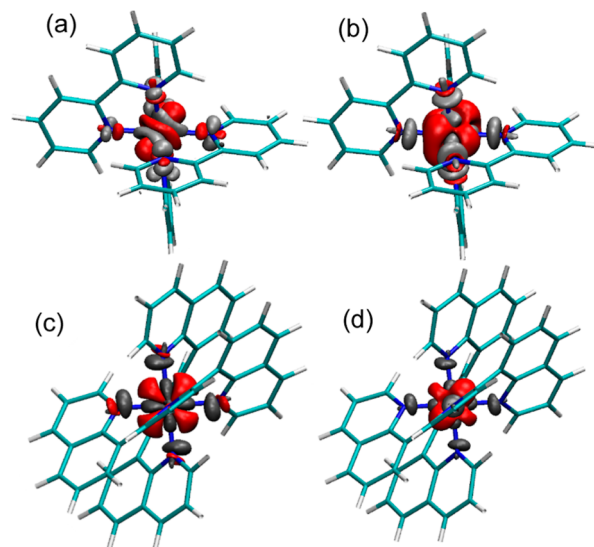


Figure 8. Change in the electron density for ${}^1S_0 \rightarrow {}^3T_1$ [left column: **C0** (a) and **C1** (c)] and ${}^1S_0 \rightarrow {}^5Q_1$ [(right column: **C0** (b) and **C1** (d)] transition calculated from quantum chemical simulations. Dark gray color is associated with charge accumulation, while red color shows charge depletion.

accumulation, while red color shows charge depletion. For **C0** (see Figure 8a,b), we find clear differences in electron density at the central iron atom between 3T_1 and 5Q_1 . On the other hand, changes at the coordinating nitrogen atoms are very similar for 3T_1 and 5Q_1 . Contrarily, for **C1** (see Figure 8c,d), the differences in electron density between 3T_1 and 5Q_1 at the central iron atom are less pronounced, while the coordinating nitrogen atoms are more affected. We find that for the 3T_1 state, the axial nitrogen atoms N2 and N2' exhibit almost no changes, while the radial coordinating nitrogen atoms N1, N1' and N3, N3' show an accumulation of charge at the nitrogen atoms. On the other hand, for the 5Q_1 state, we see a charge accumulation at all six nitrogen atoms. We assume that the differences in electron densities are likely attributed to the asymmetry in the coordination sphere, where the N2 and N2' are two single pyridine rings, while the N1, N1' and N3, N3' belong to quinolines. These differences in charge accumulation are clearly reflected in the calculated equilibrium Fe–N bond distance (see Table 1). For the 3T_1 state, we observe an increase of bond length for N1–Fe, N1'–Fe and N3–Fe, N3'–Fe, while the bond length of the axial nitrogens N2–Fe and N2'–Fe remains almost unchanged; however, for the 5Q_1 state, the bond length increases for all six nitrogen bonds.

CONCLUSIONS

Here, we demonstrate that ultrafast mid-IR spectroscopy supported by state-of-the-art quantum chemical calculations allows for a clear assignment of transient spin multiplicities of MC states in iron transition-metal complexes. For **C0**, which is a benchmark system for iron transition-metal complexes, we show that despite the subtle differences between 3T_1 and 5Q_1 state equilibrium geometries, the comparison of experimental with calculated difference spectra of the 3T_1 and 5Q_1 states allows a clear assignment toward the 5Q_1 state, in agreement with previous reports.^{25,30} For **C1**, we report a first unambiguous assignment of the long-lived MC state, ascribing it to 5Q_1 . In the case of **C1**, the quantum chemical calculations exhibit differences in axial electron densities between the 3T_1 state and the 5Q_1 state, altering transition dipole moments of vibrational modes and their frequencies. This gives rise to clear spin-sensitive marker bands at 1570–1620 cm^{-1} and 1200 cm^{-1} . Differences in the axial electron densities are likely attributed to asymmetry in the coordination sphere of **C1**. Here, the axial coordination of N2 and N2' is given by two single pyridine rings, while the other 4 coordinating Ns' belong to quinolines.

Besides the determination of the multiplicities of the long-lived MC state, investigation of the transient mid-IR dynamics provides direct insight into structural changes and tracing of energy redistribution and relaxation of excess energy processes. The presented infrared data for both complexes **C0** and **C1** reveal an increase of oscillator strength in the excited state on a sub-200 fs timescale. We attribute this change in oscillator strength to rearrangement of the ligand geometry with deviating bond lengths and partial charge distribution, accompanying the MLCT \rightarrow MC deactivation. This suggests that the flexibility in the ligand sphere allows for the stabilization of high spin states and decreases the MLCT lifetime. Our results thus support the conclusion of Darari and co-workers,¹⁹ suggesting that a higher flexibility in the ligand sphere compromises the possible effects of enhanced ligand-field splitting, stabilizing the MC state and shortening the MLCT lifetime. In addition, this aligns well with reports of significantly increased MLCT lifetimes of 528 ps¹⁴ and even up to nanoseconds²² for more rigid complexes.

Inspection of the early dynamics of **C0** and **C1** shows coherent oscillations of the breathing modes of the Fe–N coordination sphere. For **C0**, we find oscillations with 61–121 cm^{-1} , in line with previous studies,^{26,34,54} while for **C1**, we find small coherent oscillations yielding frequencies of 40–80 cm^{-1} and 150–200 cm^{-1} , matching possible low-frequency modes of our quantum chemical calculations. Moreover, transient mid-IR spectra allow for the direct observation of vibrational relaxation dynamics. Even though **C0** was well investigated by applying different kinds of state-of-the-art spectroscopic methods, to our knowledge, a direct observation of vibrational relaxation dynamics was yet not reported. On the other hand, for **C1**, vibrational relaxation processes could not be fully resolved in ultrafast UV–VIS probe experiments.¹⁹ For both complexes **C0** and **C1**, our results show clear nonexponential cooling dynamics, associated with redistribution of excess energy within the complex and dissipation into low-frequency modes. This is reflected in spectral blue shifts and narrowing of bands, with 10–20 ps.

In conclusion, ultrafast mid-IR spectroscopy together with quantum chemical calculations proves to be a readily accessible

method for the investigation of transient high spin states in metal–organic iron complexes and determination of their multiplicity. Moreover, ultrafast mid-IR spectroscopy provides critical structural information about the photophysical dynamics in metal–organic iron complexes, essential for developing efficient photosynthesizing complexes.

ASSOCIATED CONTENT

Data Availability Statement

Data for this paper, including transient polarization resolved data and calculations, are available at <https://box.fu-berlin.de/s/3jjmfKHFTXXNYdp>.

Supporting Information

The Supporting Information is available free of charge at <https://pubs.acs.org/doi/10.1021/jacs.4c01637>.

Polarization resolved data, detailed vibrational dynamics in the fingerprint region, femtosecond VIS-pump/VIS-probe data, FTIR spectra, detailed results of quantum chemical calculations, and description of selected low-frequency modes (PDF)

AUTHOR INFORMATION

Corresponding Authors

Clark Zahn – Department of Physics, Free University Berlin, D-14195 Berlin, Germany; orcid.org/0000-0002-7881-208X; Phone: +49 30 838 56107; Email: clark.zahn@fu-berlin.de

Karsten Heyne – Department of Physics, Free University Berlin, D-14195 Berlin, Germany; orcid.org/0000-0002-3243-9160; Email: karsten.heyne@physik.fu-berlin.de

Authors

Mariachiara Pastore – Université de Lorraine, CNRS, LPCT, F-54000 Nancy, France; orcid.org/0000-0003-4793-1964

J. Luis Perez Lustres – Department of Physics, Free University Berlin, D-14195 Berlin, Germany

Philippe C. Gros – Université de Lorraine, CNRS, L2CM, F-54000 Nancy, France; orcid.org/0000-0003-4905-1581

Stefan Haacke – Université de Strasbourg—CNRS, IPCMS, 67034 Strasbourg, France

Complete contact information is available at: <https://pubs.acs.org/10.1021/jacs.4c01637>

Notes

The authors declare no competing financial interest.

ACKNOWLEDGMENTS

The L2CM thanks the French Agence Nationale de la Recherche (ANR-16-CE07-0013-02) and is grateful to E. Giannoudis for providing a sample of complex **C1**. We thank the DFG for financial support (project no. 490942819).

REFERENCES

- (1) Gust, D.; Moore, T. A.; Moore, A. L. Solar Fuels via Artificial Photosynthesis. *Acc. Chem. Res.* **2009**, *42*, 1890–1898.
- (2) Hagfeldt, A.; Boschloo, G.; Sun, L.; Kloo, L.; Pettersson, H. Dye-Sensitized Solar Cells. *Chem. Rev.* **2010**, *110*, 6595–6663.
- (3) Reddy-Marri, A.; Marchini, E.; Cabanes, V. D.; Argazzi, R.; Pastore, M.; Caramori, S.; Gros, P. C. Panchromatic Light Harvesting and Record Power Conversion Efficiency for Carboxylic/Cyanoacrylic Fe(II) NHC Co-Sensitized FeSSCs. *Chem. Sci.* **2023**, *14*, 4288–4301.

- (4) Lindh, L.; Chábera, P.; Rosemann, N. W.; Uhlrig, J.; Wärnmark, K.; Yartsev, A.; Sundström, V.; Persson, P. Photophysics and Photochemistry of Iron Carbene Complexes for Solar Energy Conversion and Photocatalysis. *Catalysts* **2020**, *10*, 315.
- (5) Vos, J. G.; Kelly, J. M. Ruthenium Polypyridyl Chemistry; from Basic Research to Applications and Back Again. *Dalton Trans.* **2006**, 4869–4883.
- (6) Happ, B.; Winter, A.; Hager, M. D.; Schubert, U. S. Photogenerated Avenues in Macromolecules Containing Re(I), Ru(II), Os(II), and Ir(III) Metal Complexes of Pyridine-Based Ligands. *Chem. Soc. Rev.* **2012**, *41*, 2222–2255.
- (7) Liu, Y.; Harlang, T.; Canton, S. E.; Chábera, P.; Suárez-Alcántara, K.; Fleckhaus, A.; Vithanage, D. A.; Göransson, E.; Corani, A.; Lomoth, R.; Sundström, V.; Wärnmark, K. Towards Longer-Lived Metal-to-Ligand Charge Transfer States of Iron(II) Complexes: An N-Heterocyclic Carbene Approach. *Chem. Commun.* **2013**, *49*, 6412–6414.
- (8) Duchanois, T.; Etienne, T.; Cebrián, C.; Liu, L.; Monari, A.; Beley, M.; Assfeld, X.; Haacke, S.; Gros, P. C. An Iron-Based Photosensitizer with Extended Excited-State Lifetime: Photophysical and Photovoltaic Properties. *Eur. J. Inorg. Chem.* **2015**, *2015*, 2469–2477.
- (9) Harlang, T. C. B.; Liu, Y.; Gordivska, O.; Fredin, L. A.; Ponceca, C. S.; Huang, P.; Chábera, P.; Kjaer, K. S.; Mateos, H.; Uhlrig, J.; et al. Iron Sensitizer Converts Light to Electrons with 92% Yield. *Nat. Chem.* **2015**, *7*, 883–889.
- (10) Liu, L.; Duchanois, T.; Etienne, T.; Monari, A.; Beley, M.; Assfeld, X.; Haacke, S.; Gros, P. C. A New Record Excited State 3MLCT Lifetime for Metalorganic Iron(II) Complexes. *Phys. Chem. Chem. Phys.* **2016**, *18*, 12550–12556.
- (11) Fatur, S. M.; Shepard, S. G.; Higgins, R. F.; Shores, M. P.; Damrauer, N. H. A Synthetically Tunable System to Control MLCT Excited-State Lifetimes and Spin States in Iron(II) Polypyridines. *J. Am. Chem. Soc.* **2017**, *139*, 4493–4505.
- (12) Duchanois, T.; Liu, L.; Pastore, M.; Monari, A.; Cebrián, C.; Trolez, Y.; Darari, M.; Magra, K.; Francés-Monerris, A.; Domenichini, E.; Beley, M.; Assfeld, X.; Haacke, S.; Gros, P. C. NHC-Based Iron Sensitizers for DSSCs. *Inorganics* **2018**, *6*, 63.
- (13) Francés-Monerris, A.; Magra, K.; Darari, M.; Cebrián, C.; Beley, M.; Domenichini, E.; Haacke, S.; Pastore, M.; Assfeld, X.; Gros, P. C.; Monari, A. Synthesis and Computational Study of a Pyridylcarbene Fe(II) Complex: Unexpected Effects of fac/mer Isomerism in Metal-to-Ligand Triplet Potential Energy Surfaces. *Inorg. Chem.* **2018**, *57*, 10431–10441.
- (14) Chábera, P.; Kjaer, K. S.; Prakash, O.; Honarfar, A.; Liu, Y.; Fredin, L. A.; Harlang, T. C. B.; Lidin, S.; Uhlrig, J.; Sundström, V.; Lomoth, R.; Persson, P.; Wärnmark, K. Fe(II) Hexa N-Heterocyclic Carbene Complex with a 528 ps Metal-to-Ligand Charge-Transfer Excited-State Lifetime. *J. Phys. Chem. Lett.* **2018**, *9*, 459–463.
- (15) Magra, K.; Domenichini, E.; Francés-Monerris, A.; Cebrián, C.; Beley, M.; Darari, M.; Pastore, M.; Monari, A.; Assfeld, X.; Haacke, S.; Gros, P. C. Impact of the fac/mer Isomerism on the Excited-State Dynamics of Pyridyl-Carbene Fe(II) Complexes. *Inorg. Chem.* **2019**, *58*, 5069–5081.
- (16) Steube, J.; Burkhardt, L.; Pöpcke, A.; Moll, J.; Zimmer, P.; Schoch, R.; Wölper, C.; Heinze, K.; Lochbrunner, S.; Bauer, M. Excited-State Kinetics of an Air-Stable Cyclometalated Iron(II) Complex. *Chem.—Eur. J.* **2019**, *25*, 11826–11830.
- (17) Braun, J.; Lozada, I.; Kolodziej, C.; Burda, C.; Newman, K.; Van Lierop, J.; Davis, R.; Herbert, D. Iron(II) Coordination Complexes with Panchromatic Absorption and Nanosecond Charge-Transfer Excited State Lifetimes. *Nat. Chem.* **2019**, *11*, 1144–1150.
- (18) Tang, Z.; Chang, X.-Y.; Wan, Q.; Wang, J.; Ma, C.; Law, K.-C.; Liu, Y.; Che, C.-M. Bis(tridentate) Iron(II) Complexes with a Cyclometalating Unit: Photophysical Property Enhancement with Combinatorial Strong Ligand Field Effect. *Organometallics* **2020**, *39*, 2791–2802.
- (19) Darari, M.; Francés-Monerris, A.; Marekha, B.; Doudouh, A.; Wenger, E.; Monari, A.; Haacke, S.; Gros, P. C. Towards Iron(II) Complexes with Octahedral Geometry: Synthesis, Structure and Photophysical Properties. *Molecules* **2020**, *25*, 5991.
- (20) Magra, K.; Darari, M.; Domenichini, E.; Francés-Monerris, A.; Cebrián, C.; Beley, M.; Pastore, M.; Monari, A.; Assfeld, X.; Haacke, S.; Gros, P. C. Photophysical Investigation of Iron(II) Complexes Bearing Bidentate Annulated Isomeric Pyridine-NHC Ligands. *J. Phys. Chem. C* **2020**, *124*, 18379–18389.
- (21) Vittardi, S. B.; Magar, R. T.; Schrage, B. R.; Ziegler, C. J.; Jakubikova, E.; Rack, J. J. Evidence for a Lowest Energy 3MLCT Excited State in $[\text{Fe}(\text{tpy})(\text{CN})_3]^-$. *Chem. Commun.* **2021**, *57*, 4658–4661.
- (22) Leis, W.; Argüello Cordero, M. A.; Lochbrunner, S.; Schubert, H.; Berkefeld, A. A Photoreactive Iron(II) Complex Luminophore. *J. Am. Chem. Soc.* **2022**, *144*, 1169–1173.
- (23) Moll, J.; Förster, C.; König, A.; Carrella, L. M.; Wagner, M.; Panthöfer, M.; Möller, A.; Rentschler, E.; Heinze, K. Panchromatic Absorption and Oxidation of an Iron(II) Spin Crossover Complex. *Inorg. Chem.* **2022**, *61*, 1659–1671.
- (24) Creutz, C.; Chou, M.; Netzel, T. L.; Okumura, M.; Sutin, N. Lifetimes, Spectra, and Quenching of the Excited States of Polypyridine Complexes of Iron(II), Ruthenium(II), and Osmium(II). *J. Am. Chem. Soc.* **1980**, *102*, 1309–1319.
- (25) Gawelda, W.; Cannizzo, A.; Pham, V.-T.; van Mourik, F.; Bressler, C.; Chergui, M. Ultrafast Nonadiabatic Dynamics of $[\text{Fe}^{\text{II}}(\text{bpy})_3]^{2+}$ in Solution. *J. Am. Chem. Soc.* **2007**, *129*, 8199–8206.
- (26) Auböck, G.; Chergui, M. Sub-50-fs Photoinduced Spin Crossover in $[\text{Fe}(\text{bpy})_3]^{2+}$. *Nat. Chem.* **2015**, *7*, 629–633.
- (27) Abrahamsson, M.; Jäger, M.; Österman, T.; Eriksson, L.; Persson, P.; Becker, H.-C.; Johansson, O.; Hammarström, L. A 3.0 microsecond Room Temperature Excited State Lifetime of a Bistridentate Ru(II)-Polypyridine Complex for Rod-like Molecular Arrays. *J. Am. Chem. Soc.* **2006**, *128*, 12616–12617.
- (28) Mengel, A. K. C.; Förster, C.; Breivogel, A.; Mack, K.; Ochsmann, J. R.; Laquai, F.; Ksenofontov, V.; Heinze, K. A Heteroleptic Push–Pull Substituted Iron(II) Bis(tridentate) Complex with Low-Energy Charge-Transfer States. *Chem.—Eur. J.* **2015**, *21*, 704–714.
- (29) Britz, A.; Gawelda, W.; Assefa, T. A.; Jamula, L. L.; Yarranton, J. T.; Galler, A.; Khakhulin, D.; Diez, M.; Harder, M.; Doumy, G.; et al. Using Ultrafast X-ray Spectroscopy to Address Questions in Ligand-Field Theory: The Excited State Spin and Structure of $[\text{Fe}(\text{dcp})_2]^{2+}$. *Inorg. Chem.* **2019**, *58*, 9341–9350.
- (30) Smeigh, A. L.; Creelman, M.; Mathies, R. A.; McCusker, J. K. Femtosecond Time-Resolved Optical and Raman Spectroscopy of Photoinduced Spin Crossover: Temporal Resolution of Low-to-High Spin Optical Switching. *J. Am. Chem. Soc.* **2008**, *130*, 14105–14107.
- (31) Consani, C.; Prémont-Schwarz, M.; ElNahas, A.; Bressler, C.; van-Mourik, F.; Cannizzo, A.; Chergui, M. Vibrational Coherences and Relaxation in the High-Spin State of Aqueous $[\text{Fe}^{\text{II}}(\text{bpy})_3]^{2+}$. *Angew. Chem.* **2009**, *48*, 7184–7187.
- (32) Zhang, W.; Alonso-Mori, R.; Bergmann, U.; Bressler, C.; Chollet, M.; Galler, A.; Gawelda, W.; Hadt, R. G.; Hartssock, R. W.; Kroll, T.; et al. Tracking Excited-State Charge and Spin Dynamics in Iron Coordination Complexes. *Nature* **2014**, *509*, 345–348.
- (33) Haldrup, K.; Gawelda, W.; Abela, R.; Alonso-Mori, R.; Bergmann, U.; Bordage, A.; Cammarata, M.; Canton, S. E.; Dohn, A. O.; van Driel, T. B.; et al. Observing Solvation Dynamics with Simultaneous Femtosecond X-ray Emission Spectroscopy and X-ray Scattering. *J. Phys. Chem. B* **2016**, *120*, 1158–1168.
- (34) Lemke, H.; Kjaer, K.; Hartssock, R.; Van Driel, T.; Chollet, M.; Glowia, J.; Song, S.; Zhu, D.; Pace, E.; Matar, S.; Nielsen, M.; Benfatto, M.; Gaffney, K.; Collet, E.; Cammarata, M. Coherent Structural Trapping Through Wave Packet Dispersion during Photoinduced Spin State Switching. *Nat. Commun.* **2017**, *8*, 15342.
- (35) Carey, M. C.; Adelman, S.; McCusker, J. K. Insights into the Excited State Dynamics of Fe(II) Polypyridyl Complexes from Variable-Temperature Ultrafast Spectroscopy. *Chem. Sci.* **2019**, *10*, 134–144.

- (36) Miller, J. N.; McCusker, J. K. Outer-Sphere Effects on Ligand-Field Excited-State Dynamics: Solvent Dependence of High-Spin to Low-Spin Conversion in $[\text{Fe}(\text{bpy})_3]^{2+}$. *Chem. Sci.* **2020**, *11*, 5191–5204.
- (37) Jiang, Y.; Liu, L.; Sarracini, A.; Krawczyk, K.; Wentzell, J.; Lu, C.; Field, R.; Matar, S.; Gawelda, W.; Müller-Werkmeister, H. M.; Miller, R. Direct Observation of Nuclear Reorganization Driven by Ultrafast Spin Transitions. *Nat. Commun.* **2020**, *11*, 1530.
- (38) Oppermann, M.; Zinna, F.; Lacour, J.; Chergui, M. Chiral Control of Spin-Crossover Dynamics in Fe(II) Complexes. *Nat. Chem.* **2022**, *14*, 739–745.
- (39) Wolf, M. M. N.; Groß, R.; Schumann, C.; Wolny, J. A.; Schünemann, V.; Døssing, A.; Paulsen, H.; McGarvey, J. J.; Diller, R. Sub-Picosecond Time Resolved Infrared Spectroscopy of High-Spin State Formation in Fe(II) Spin Crossover Complexes. *Phys. Chem. Chem. Phys.* **2008**, *10*, 4264–4273.
- (40) Mukuta, T.; Tanaka, S.; Inagaki, A.; Koshihara, S. y.; Onda, K. Direct Observation of the Triplet Metal-Centered State in $[\text{Ru}(\text{bpy})_3]^{2+}$ Using Time-Resolved Infrared Spectroscopy. *ChemistrySelect* **2016**, *1*, 2802–2807.
- (41) Sun, Q.; Dereka, B.; Vauthey, E.; Lawson Daku, L. M.; Hauser, A. Ultrafast Transient IR Spectroscopy and DFT Calculations of Ruthenium(II) Polypyridyl Complexes. *Chem. Sci.* **2017**, *8*, 223–230.
- (42) Bouzaid, J.; Schultz, M.; Lao, Z.; Bartley, J.; Bostrom, T.; McMurtrie, J. Supramolecular Selection in Molecular Alloys. *Cryst. Growth Des.* **2012**, *12*, 3906–3916.
- (43) Kaindl, R. A.; Wurm, M.; Reimann, K.; Hamm, P.; Weiner, A. M.; Woerner, M. Generation, Shaping, and Characterization of Intense Femtosecond Pulses Tunable from 3 to 20 μm . *J. Opt. Soc. Am.* **2000**, *17*, 2086–2094.
- (44) Stensitzki, T. Femtosecond Pump-Probe Spectroscopy on Corroles, Phytochromes, Channelrhodopsins and Ground-state Reactions. Ph.D. Thesis, Department of Physics, Freie Universität Berlin, 2019.
- (45) Stensitzki, T. *Skultrafast—A Python Package for Time-Resolved Spectroscopy*, 2021.
- (46) Grimme, S.; Antony, J.; Ehrlich, S.; Krieg, H. A Consistent and Accurate Ab Initio Parametrization of Density Functional Dispersion Correction (DFT-D) for the 94 Elements H-Pu. *J. Chem. Phys.* **2010**, *132*, 154104.
- (47) Frisch, M. J.; et al. *Gaussian 16*. Revision C.01; Gaussian Inc.: Wallingford CT, 2016.
- (48) Wallin, S.; Davidsson, J.; Modin, J.; Hammarstrom, L. Femtosecond Transient Absorption Anisotropy Study on $[\text{Ru}(\text{bpy})_3]^{2+}$ and $[\text{Ru}(\text{bpy})(\text{py})_4]^{2+}$. Ultrafast Interligand Randomization of the MLCT State. *J. Phys. Chem. A* **2005**, *109*, 4697–4704.
- (49) Stensitzki, T.; Yang, Y.; Berg, A.; Mohammed, A.; Gross, Z.; Heyne, K. Ultrafast Electronic and Vibrational Dynamics in Brominated Aluminum Corroles: Energy Relaxation and Triplet Formation. *Struct. Dynam.* **2016**, *3*, 043210.
- (50) Zahn, C.; Stensitzki, T.; Heyne, K. Femtosecond Anisotropy Excitation Spectroscopy to Disentangle the Q_x and Q_y Absorption in Chlorophyll *a*. *Chem. Sci.* **2022**, *13*, 12426–12432.
- (51) Hamm, P.; Ohline, S. M.; Zinth, W. Vibrational Cooling After Ultrafast Photoisomerization of Azobenzene Measured by Femtosecond Infrared Spectroscopy. *J. Chem. Phys.* **1997**, *106*, 519–529.
- (52) Kovalenko, S. A.; Schanz, R.; Hennig, H.; Ernsting, N. P. Cooling Dynamics of an Optically Excited Molecular Probe in Solution from Femtosecond Broadband Transient Absorption Spectroscopy. *J. Chem. Phys.* **2001**, *115*, 3256–3273.
- (53) Marciniak, H.; Lochbrunner, S. On the Interpretation of Decay Associated Spectra in the Presence of Time Dependent Spectral Shifts. *Chem. Phys. Lett.* **2014**, *609*, 184–188.
- (54) Zhang, K.; Ash, R.; Girolami, G. S.; Vura-Weis, J. Tracking the Metal-Centered Triplet in Photoinduced Spin Crossover of Fe(phen) $^{32+}$ with Tabletop Femtosecond M-Edge X-ray Absorption Near-Edge Structure Spectroscopy. *J. Am. Chem. Soc.* **2019**, *141*, 17180–17188.